PHYSICAL REVIEW MATERIALS **3**, 064003 (2019)

Stacking, strain, and twist in 2D materials quantified by 3D electron diffraction

Suk Hyun Sung,[1] Noah Schnitzer,[1] Lola Brown,[2] Jiwoong Park,[3,4,5] and Robert Hovden[1,6,*]
[1] *Department of Materials Science and Engineering, University of Michigan, Ann Arbor, Michigan 48109, USA*
[2] *Intel Electronics, Kiryat Gat 82109, Israel*
[3] *Department of Chemistry, University of Chicago, Chicago, Illinois 60637, USA*
[4] *Institute for Molecular Engineering, University of Chicago, Chicago, Illinois 60637, USA*
[5] *James Franck Institute, University of Chicago, Chicago, Illinois 60637, USA*
[6] *Applied Physics Program, University of Michigan, Ann Arbor, Michigan 48109, USA*

(Received 11 March 2019; published 25 June 2019)

The field of two-dimensional (2D) materials has expanded to multilayered systems in which electronic, optical, and mechanical properties change—often dramatically—with stacking order, thickness, twist, and interlayer spacing. For transition metal dichalcogenides (TMDs), bond coordination within a single van der Waals layer changes the out-of-plane symmetry that can cause metal-insulator transitions or emergent quantum behavior. Discerning these structural order parameters is often difficult using real-space measurements; however, we show that 2D materials have distinct, conspicuous three-dimensional (3D) structure in reciprocal space described by nearly infinite oscillating Bragg rods. Combining electron diffraction and specimen tilt we probe Bragg rods in all three dimensions to identify multilayer structure with subangstrom precision across several 2D materials—including TMDs (MoS_2, $TaSe_2$, TaS_2) and multilayer graphene. We demonstrate quantitative determination of key structural parameters such as surface roughness, inter- and intralayer spacings, stacking order, and interlayer twist using a rudimentary transmission electron microscope. We accurately characterize the full interlayer stacking order of multilayer graphene (1, 2, 6, 12 layers) as well the intralayer structure of MoS_2 and extract a chalcogen-chalcogen layer spacing of 3.07 ± 0.11 Å. Furthermore, we demonstrate quick identification of multilayer rhombohedral graphene.

DOI: 10.1103/PhysRevMaterials.3.064003

I. INTRODUCTION

The characteristics of layered two-dimensional (2D) materials and heterostructures are intimately linked with stacking order, as thickness and interlayer registry dramatically alter the confinement and symmetry of the system. For instance, inversion-symmetric monolayer $1T$-MoS_2 is metallic [1] while mirror-symmetric monolayer $2H$-MoS_2 is a direct band gap semiconductor [2]. In several 2D systems, the intrinsic inversion asymmetry or symmetry breaking via external perturbation bear possibilities for electronic switching [3,4] or valleytronic devices [5]. Recently, superconductivity was observed in bilayer graphene when the interlayer twist is tuned to a "magic angle" [6].

High-precision characterization of stacking order, interlayer spacing, twist, and roughness is paramount to harnessing the diversity of 2D phenomena. The field of 2D materials erupted with facile identification of single-layer graphene when exfoliated onto ~300-nm-thick SiO_2 substrates [7]. Since then, thickness characterization techniques have expanded to Raman spectroscopy [8], atomic force microscopy [9], and electron microscopy [10]. Thickness alone, however, provides an incomplete picture of the atomic structure and stacking order. Scanning transmission electron microscopy (STEM) can image thickness with atomic resolution [11,12], yet, this real-space projection of the specimen loses out-of-plane information, poorly discerns light elements bonded to heavy elements, and requires high radiation doses. Furthermore, a fundamental trade-off between resolution and field of view limits atomic-resolution imaging to small regions of interest, typically $(20\ \mathrm{nm})^2$. In contrast, electron diffraction remains a longstanding powerful tool for obtaining a representative average of the atomic structure across large areas, at lower doses, with high-throughput and high precision.

We demonstrate that electron diffraction is particularly apt for probing the three-dimensional (3D) structure of 2D materials. Contrary to the confined real-space structure, we show that 2D materials have striking, measurable features in the third dimension of reciprocal space that describe key structural parameters such as stacking order, twist, strain, chemistry, and inter- or intralayer spacing. In 2D materials, Bragg peaks extend into nearly infinite rods running perpendicular to the specimen surface. Each Bragg rod oscillates with intensity and phase described by the atomic arrangement within and between each 2D layer.

Prominent distinctions arise in the reciprocal (k) space structure of 2D materials: (a) In-plane lattice strain moves the position of Bragg rods. (b) Rod oscillation frequencies are inversely proportional to inter- and intralayer spacing. (c) Out-of-plane strain changes the oscillation frequency. (d) Symmetry and structure of first-order rods (Γ_1) reveal stacking order. (d) Second-order rods (Γ_2) facilitate thickness determina-

---

[*] hovden@umich.edu

2475-9953/2019/3(6)/064003(8)

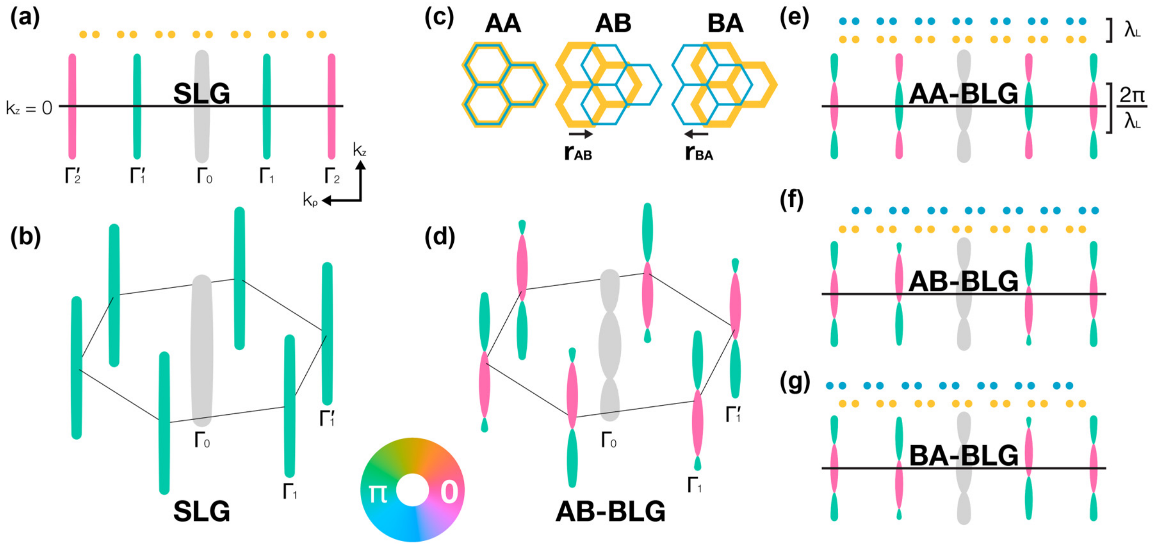

FIG. 1. 3D reciprocal structure of single and bilayer graphene. 3D reciprocal-space structure of (a), (b) single-layer graphene (SLG). Width and color of Bragg rods indicate magnitude and phase (magenta = 0, teal = π); the hexagon marks $k_z = 0$ plane. (c) Bilayer graphene (BLG) illustrated for AA, AB, and BA registry along $\hat{\mathbf{z}}$. (d) 3D k-space structure of AB-BLG. Sinusoidal magnitude—signature of multilayer systems—is apparent. The structures of (e) AA, (f) AB, and (g) BA from side view are shown for both first (Γ_1) and second (Γ_2) order Bragg rods along with atomic stacking along ⟨100⟩ direction in real space. The barely visible decay in rod magnitude seen in SLG is due to the finite size of carbon atoms. The rod structures of BLGs are sinusoidal with symmetry identical to the real space. Sixfold symmetry of SLG and inversion symmetry of Bernal BLG are clearly shown in k space. All structures are centered around the inversion center in real space to maximize interpretability.

tion. (e) Chemistry changes the amplitude of oscillations. (f) Twisted layers are described by a superposition of diffraction patterns for nonoverlapping (incommensurate) Bragg rods. (g) Progressive broadening of rods is associated with out-of-plane microcorrugation and stiffness. (h) Curvature of the Ewald sphere results in a small, measurable excitation error in the diffraction pattern that breaks expected Friedel symmetry.

Combining specimen tilt and diffraction, we construct "diffraction tilt patterns" that measure the 3D structural details of single and multilayer 2D materials. This work substantially extends previous work for few-layer graphene [13,14] and boron nitride [15] to transition metal dichalcogenides (TMDs) and multilayer materials. Furthermore, we expound the foundational details required to enable a wide-range 3D diffraction analysis across all 2D materials.

II. BACKGROUND TO DIFFRACTION OF 2D MATERIALS

The wave behavior of matter was first hypothesized by de Broglie in 1924 [16], and three years later validated by Thomson, Davisson, and Germer with the experimental demonstration of electron diffraction [17,18]. In the far field, diffracted high-energy electrons are described by a near planar slice through the specimen's 3D reciprocal structure: $V(k_z = 0)$, i.e., a Fourier transform of the projected specimen potential. This kinematic approximation [19] accurately describes diffraction of 2D materials much thinner than the mean-free path (e.g., $\ll$150 nm for 200 keV electrons in Si [20]), where multiple scattering is negligible. Tilting the specimen changes the electron beam's angle of incidence, rotating the planar slice through the reciprocal lattice to probe the 3D structure. In diffraction, only squared magnitude, $|V(\mathbf{k})|^2$, without complex phase is measured.

We are challenged to discern the third dimension of 2D materials in real and reciprocal space. Graphene is an archetypal 2D crystal in which sp^2 bonding forms a hexagonal lattice lying within a single plane. Graphene's real-space lattice, $V_g(\mathbf{r}) = \text{III}_{\mathbf{a}_1,\mathbf{a}_2}(\mathbf{r})\delta(z) \circledast \sum_j f(\mathbf{r} - \mathbf{r}_j)$, is described by two lattice vectors, $\mathbf{a}_1, \mathbf{a}_2$, with magnitude $a_g = 2.46$ Å, and a two-atom sublattice at $\mathbf{r}_j$ $(j \in 0, 1)$ that mimics a honeycomb. The corresponding reciprocal lattice of graphene defines Bragg rods spaced $b_g = \frac{4\pi}{a_g\sqrt{3}} = 2.949$ Å^{-1} apart and is described by

$$V_g(\mathbf{k}) = \text{III}_{\mathbf{b}_1,\mathbf{b}_2}(\mathbf{k}) \cdot S_g(\mathbf{k}), \tag{1}$$

where the complex magnitude is determined by structure factor $S_g(\mathbf{k}) = \sum_j f(\mathbf{k})e^{-i\mathbf{k}\cdot\mathbf{r}_j}$. For graphene, the single atomic plane, with nearly infinite confinement along $\hat{\mathbf{z}}$ [Fig. 1(a), top], has a reciprocal structure with near infinite extent out-of-plane along $\hat{\mathbf{k}}_z$ [Fig. 1(a), bottom]. Similar elongated rel-rods arise from planar shape factors [21,22] that have been studied in surface layer diffraction experiments on bulk materials and thin films [23–25]. Section II of the Supplemental Material [26] discusses $\text{III}(\mathbf{k})$ formulation and the normalization prefactor.

Therefore, 2D materials have Bragg peaks that stretch into rods. Figures 1(a) and 1(b) show single-layer graphene (SLG) in reciprocal space. Its k lattice has sixfold rotational symmetry [Fig. 1(b)], reflecting the real-space symmetry at the inversion center. The rod intensity decays slowly from the origin due to the small but finite size of each atom [described by atomic scattering factor $f(\mathbf{k})$]. The attenuating magnitude

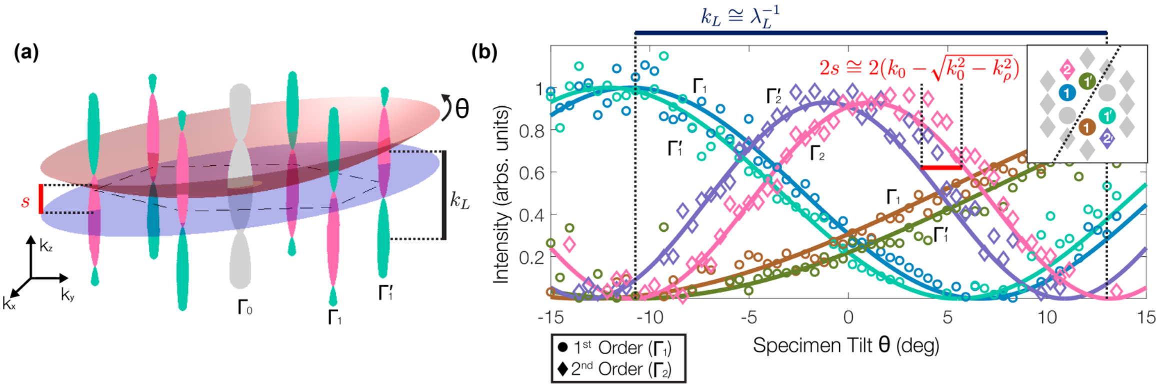

FIG. 2. Diffraction tilt patterns of BLG. (a) 3D reciprocal rod structure of Bernal-stacked bilayer graphene. The magnitude varies sinusoidally with a periodicity inversely proportional to real-space interlayer spacing ($k_L = \frac{4\pi}{\lambda_L}$). At typical TEM operation energy (blue, 200 keV), SAED is a nearly planar slice through the *k*-space origin; red surface exaggerates the curvature of Ewald sphere with slow electron (0.3 keV). Tilting the specimen in TEM column changes the beam's incident angle and effectively rocks the diffraction plane with respect to the Bragg rods, accessing out-of-plane information hidden in conventional TEM. The excitation error (s)—due to the curvature—are small but not negligible at low tilt angles close to the *k*-space origin. (b) Kinematic (solid curves) and experimental (○, ◊) tilt patterns of BLG. The tilt patterns oscillate with frequency k_L. Nontrivial Ewald sphere curvature separates analogous second-order Friedel pair tilt patterns [magenta (Γ_2) and blue (Γ_2')] with phase difference associated with s.

reaches 80% by 0.038 Å^{-1}. Both first- (Γ_1) and second-order (Γ_2) rods are shown in Fig. 1(a). For SLG, the more distant second-order Bragg rods have ~94% of the squared magnitude of the first-order rods.

Combining specimen tilt and diffraction allows quantification of each Bragg rod's 3D structure. In a "diffraction tilt pattern," diffraction peaks are quantified across specimen tilt angles. As the specimen is tilted about an axis perpendicular to the beam direction, the diffraction plane rotates through the reciprocal rods of the material as shown in Fig. 2(a) for the first-order rods of bilayer graphene. Figure 2(b) illustrates the resulting tilt pattern, and the inset notes the specimen tilt axis.

Diffraction peaks both move and broaden when a 2D crystal is tilted and must be handled during quantification. Approaching higher tilts, peaks move outward from the axis of rotation—giving the illusion of unidirectional strain. The increasing distance between Bragg peaks reflects the apparent contraction in real space when a tilted 2D crystal is viewed in projection. Thus, diffraction peaks are minimally spaced apart when the 2D crystal is perpendicular to the beam (i.e., "on-axis"). Also, the effective selected area increases as tilt increases and a geometric factor of $\cos(\theta)^{-2}$ must be incorporated into the kinematic model of diffraction of large crystals.

Bragg peaks also broaden at higher tilts due to out-of-plane rippling of the material. Meyer *et al.* quantified intrinsic microscopic roughing of graphene by measuring the Bragg rod precession [27]. Any microcorrugation in a 2D sheet has local orientation changes that tilt the Bragg rods. Because selected-area electron diffraction (SAED) measures an average of the crystal region, the superposition of tilted Bragg rods results in broadening along $\hat{\mathbf{k}}_z$. Meyer *et al.* measured Bragg rod broadening to quantify roughness of graphene and showed that suspended single-layer graphene had a surface normal that varied by ±5 degrees while bilayer graphene was smoother with a ±1 degree variation. Their work also highlights the importance of quantifying Bragg peaks from integrated intensities—not peak maxima.

III. BILAYER GRAPHENE

Atomically registered bilayer materials have Bragg rods that sinusoidally oscillate in complex magnitude [Fig. 1(d)] with periodicity ($4\pi/\lambda_L$) inversely proportional to the interlayer spacing, λ_L. The period of rod oscillation is independent of stacking order and depends only on interlayer spacing. Bilayer graphene (BLG) has reciprocal structure described by

$$\begin{aligned} V_{bg}(\mathbf{r}) = {} & [\text{III}_{\mathbf{a}_1,\mathbf{a}_2}(\mathbf{r} - \mathbf{\Delta}/2)\delta(z - \lambda_L/2) \\ & + \text{III}_{\mathbf{a}_1,\mathbf{a}_2}(\mathbf{r} + \mathbf{\Delta}/2)\delta(z + \lambda_L/2)] \\ & \circledast \textstyle\sum_i f(\mathbf{r} - \mathbf{r}_i), \end{aligned} \tag{2}$$

$$V_{bg}(\mathbf{k}) = \text{III}_{\mathbf{b}_1,\mathbf{b}_2}(\mathbf{k})\left[2\cos\left(\frac{\lambda_L}{2}k_z + \frac{\mathbf{\Delta}}{2}\cdot\mathbf{k}\right)\right]\cdot S_g(\mathbf{k}), \tag{3}$$

where $\mathbf{\Delta}$ is the order parameter representing in-plane translation.

Changes to stacking order move Bragg rods up and down along $\hat{\mathbf{k}}_z$. More specifically, in-plane displacement of a layer, $\mathbf{\Delta}$, adds a phase shift $\frac{1}{2}\mathbf{\Delta}\cdot\mathbf{k}$ to the sinusoidal intensity of each Bragg rod. There are three high-symmetry stacking configurations for BLG: energetically stable AB or BA (called Bernal or graphitic) and unstable AA [Fig. 1(c)] [28]. The arrangement of the sinusoidal rods reflects the real-space symmetry. AA-BLG is defined by two aligned layers ($\mathbf{\Delta} = 0$) with a mirror plane in between [Fig. 1(e)]. The reciprocal-space structure matches the real-space sixfold symmetry with a mirror plane at $k_z = 0$. In AB/BA-BLG, one layer is bond-length shifted with respect to the other along an in-plane bond direction ($\mathbf{\Delta} = \frac{\mathbf{a}_1+\mathbf{a}_2}{3}$) [29]. This translation breaks out-of-plane mirror symmetry and reduces the sixfold symmetry to threefold.

Figures 1(e), 1(f), and 1(g) depict the rod structure of AA, AB, and BA-BLG. The magnitude of each rod is described by its width and complex phase with color; magenta and teal represent 0 and π, respectively. Mirror-symmetric AA-BLG has first-order diffraction rods (Γ_1) centered about $k_z = 0$ [Fig. 1(c)]. For AB-BLG, the in-plane translation between atomic layers displaces Γ_1 and Γ_1' Bragg rods in opposite out-of-plane directions ($\pm\hat{\mathbf{k}}_z$) with a $\pi/3$ phase shift [Figs. 1(f) and 1(g)].

Γ_1 rods reveal stacking order in 2D materials. For Bernal BLG the maximum intensity of odd-order Bragg rods can only be measured by tilting the specimen [Fig. 2(a)]. In the experimental tilt pattern of AB-BLG [Fig. 2(b)], the nonsymmetric first-order Bragg rods are obvious. The blue Γ_1 curve decreases to zero intensity at 6 degrees tilt but reaches a maximum at -12 degrees (also expected at 23 degrees). The brown Γ_1 rod on the other side of the rotation axis follows a similar opposite trend. Bragg rods more distant from the axis of rotation oscillate more rapidly in the tilt pattern. Here the axis of rotation passes through Γ_2 as shown in Fig. 2(b), inset. In real space, the maximum intensity of Γ_1 occurs when Bernal bilayer graphene is tilted so all atoms between layers lie atop one another when viewed along the beam direction. For AB and BA the patterns are mirrored and maximum intensity occurs when tilting in opposite directions. Brown *et al.* exploited this broken symmetry using specimen tilt to quickly distinguish AB and BA domains in bilayer graphene [13]. For AA-BLG the maximum diffraction intensity trivially occurs at 0 degrees tilt.

Γ_2 rods reveal the number of layers in multilayer graphene, but not stacking order. For untilted specimens ($k_z \approx 0$), the intensity of the Γ_2 rods in the bilayer is four times that of monolayer graphene and will continue to scale with number of layers squared, N^2, as discussed in Sec. VII. Shown in Figs. 1(e)–1(g), the Γ_2 rods are identical and indiscernible for all three BLG stacking orders. Γ_2 rod intensity has a mirror-symmetric maximum at $k_z = 0$ that is clearly seen in the experimentally measured tilt pattern [Fig. 2(b)]. The slight deviation of Γ_2 maximum from zero tilt is due to finite curvature of the Ewald sphere.

IV. BEAM ENERGY AND THE EWALD SPHERE

Elastic scattering preserves kinetic energy on the proverbial Ewald sphere in reciprocal space [30]. At finite beam energies, the diffraction pattern is described by a spherical surface cutting through the reciprocal lattice. At typical TEM energies (60–300 keV), the curvature of the Ewald sphere is small but not negligible. As shown in Fig. 2(a), the Ewald sphere passes through Bragg rods slightly above the $k_z = 0$ plane (historically referred to as excitation error, s). Tilting the specimen is equivalent to tilting the Ewald sphere.

Diffraction tilt patterns come in Friedel pairs [31] composed of a Bragg rod (at $\mathbf{k}$) and its centrosymmetric pair (at $-\mathbf{k}$). For a flat Ewald sphere (infinite beam energy) the Friedel pairs have equivalent tilt patterns. However, with the Ewald sphere curvature the tilt patterns for each Friedel pair bifurcate with increasing separation at lower beam voltages (higher curvature). Figure 2(b) shows the measurable curvature of the Ewald sphere in an experimental diffraction tilt pattern of bilayer graphene. Here, curves appear in pairs offset by a few degrees. This is most clearly seen in Γ_2 diffraction [Fig. 2(b) (pink, purple)], where the maximum intensity occurs at ± 1.1 degrees. This angular distance in the split of paired tilt patterns directly measures the Ewald sphere curvature and excitation error s: $s = k_0 - \sqrt{k_0^2 - k_\rho^2}$, where k_0 is the wave number of the incident electron and k_ρ is the in-plane radial distance to k-space origin. For small tilt angles and Bragg peaks close to the k-space origin this will scale approximately linearly, while for larger angles at larger radial distances a conversion from specimen tilt to a Cartesian basis is detailed in Sec. III of the Supplemental Material [26]. Bragg rod intensity plots in k_z corresponding to Figs. 2, 5, and 6 are featured in Fig. S7 of the Supplemental Material [26]. Here, the ± 1.1 degrees split in the low-angle tilt patterns corresponds to an excitation error of 0.085 Å^{-1} at 80 keV.

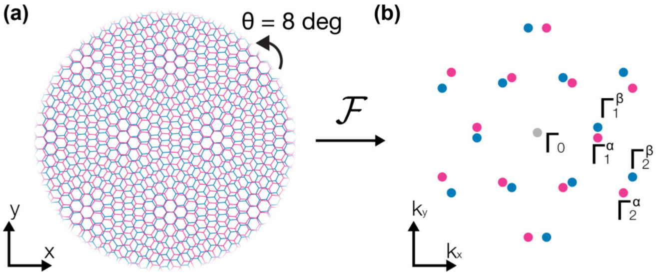

FIG. 3. Twisted bilayer graphene. (a) Twisted bilayer graphene with an incommensurate intralayer twist angle ($\theta = 8$ deg). (b) Reciprocal structure of incommensurate twisted BLG is a simple superposition of layers.

V. TWISTED, MOIRÉ LAYERS

Significant interest in twisted multilayer materials has followed the micromechanical exfoliation of 2D heterojunctions [32] and discovery of superconductivity in low-twist-angle bilayer graphene [6]. The reciprocal lattice of twisted bilayers is described by $|\mathcal{F}[\mathrm{III}_\alpha(\mathbf{r}) + \mathrm{III}_\beta(\mathbf{r})]|^2 = |\mathrm{III}_\alpha(\mathbf{k})|^2 + |\mathrm{III}_\beta(\mathbf{k})|^2 + \mathrm{III}_\alpha^*(\mathbf{k})\mathrm{III}_\beta(\mathbf{k}) + \mathrm{III}_\alpha(\mathbf{k})\mathrm{III}_\beta^*(\mathbf{k})$, for layers α and β. For incommensurate stacking, the cross term is zero and the diffraction pattern is a trivial superposition of each individual layer (Fig. 3). This allows independent characterization of each incommensurate layer; however, we lose the ability to characterize interlayer spacing. If α and β are commensurate [33], the cross term is zero where the Bragg rods from each layer do not overlap. Only overlapping rods may interfere and sinusoidally oscillate. As shown by Brown *et al.*, each twisted layer can be independently mapped in real space with dark-field TEM by placing an aperture around each distinct Bragg peak in the diffraction plane of the TEM [13].

Yoo *et al.* recently reported that at low twist angles (<3 deg) in bilayer graphene periodic restructuring occurs and superlattice peaks emerge [34]. Systems with periodic lattice distortions, either from interlayer interaction or charge order, are not so simply described as a superposition of layers [35].

VI. 2D TRANSITION METAL DICHALCOGENIDES

Transition metal dichalcogenides (TMDs) are composed of three atomic planes and two chemical species within each van der Waals (vdW) layer that add complexity to the

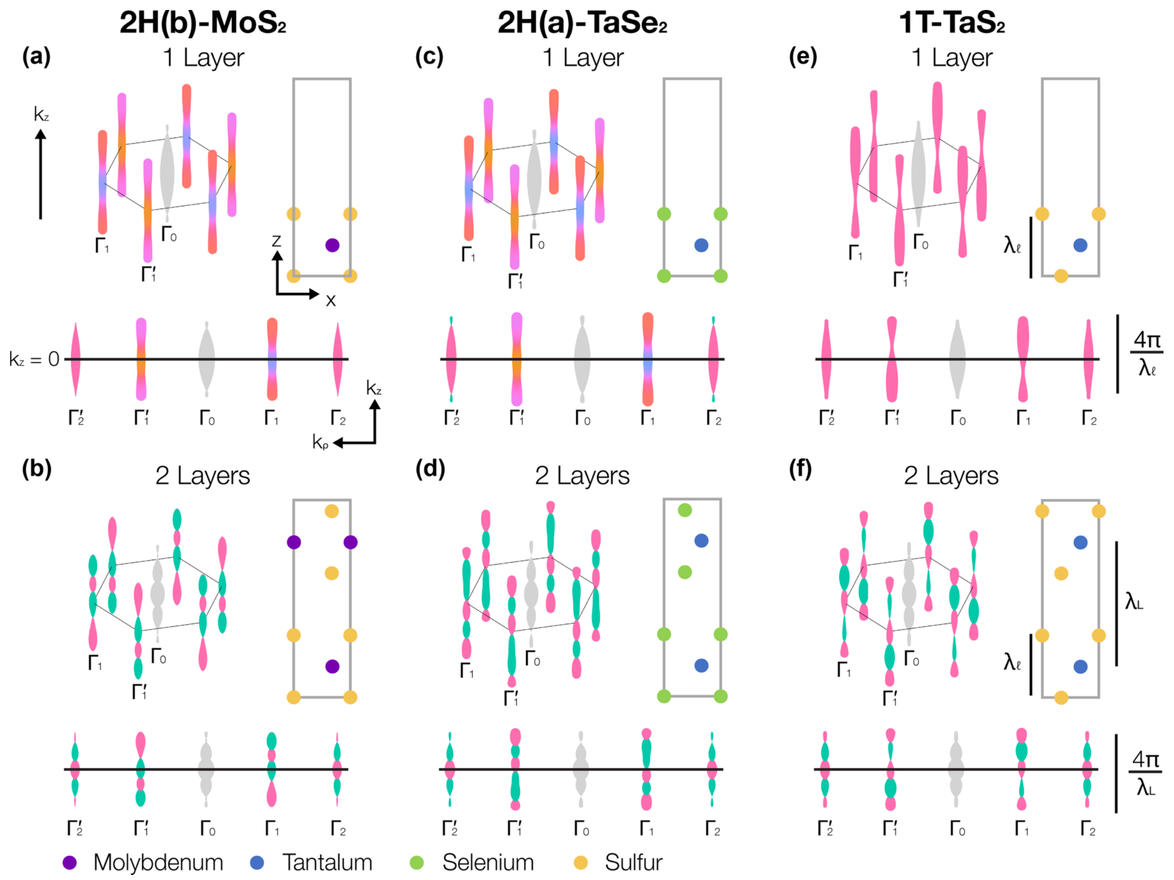

FIG. 4. 3D reciprocal structure of 2D transition metal dichalcogenides and polytypes. For each TMD, the Bragg rods (Γ_0, Γ_1) are shown in 3D alongside a real-space $\langle 100 \rangle$ projection of the crystal stacking order. Below, a side view of the Bragg rods (Γ_0, Γ_1, Γ_2) quantitatively illustrates the structure in k space. Bragg rods have thickness and color indicating the complex magnitude and phase, respectively. For single-layer TMDs [(a), (c), (e)], two sinusoidal oscillations are determined by the interlayer spacing of the three atomic planes. The complexity increases noticeably for two vdW layers [(b), (d), (f)], which includes a beating frequency from interlayer spacing. Noticeably, H-phase MoS_2 and $TaSe_2$ have different stable multilayer stacking, denoted $2H$(b) and $2H$(a), leading to drastically different Bragg rod contours.

Bragg rod structure [Figs. 4(a), 4(c), and 4(e) (top)]. Six chalcogens encapsulate each metal atom geometrically with two tetrahedrons. Single-layer TMDs are categorized into hexagonal H or trigonal T polytype phases by this local metal-chalcogen coordination complex [36]. In the H phase, the two tetrahedrons align along $\hat{\mathbf{z}}$ [Fig. 4(a)], and in the T phase, the two are displaced by 30 degrees giving rise to inversion symmetry [Fig. 4(e)]. Although isomeric to the $1T$, the $2H$ phase notably breaks this inversion symmetry within a single layer but regains it in the bilayer. Broken inversion symmetry can significantly change electronic structure and has been associated with a metal-insulator transition in the $1T \rightarrow 2H$ transformation [1,2] and the indirect to direct band gap transition in $2H$ TMDs reduced to a single layer ($1H$) [2]. In several TMDs, such as TaS_2 and $TaSe_2$, the $1T$ phase permits room temperature charge ordering and even superconductivity at higher pressures [37].

Diffraction combined with specimen tilt can precisely determine metal-chalcogen coordination within a single vdW layer due to its sensitivity to crystal symmetry. The three atomic planes composing a vdW layer are described by Bragg rods oscillating with a periodicity inversely proportional to λ_ℓ, the intralayer spacing between chalcogen-chalcogen atomic planes:

$$V_{1H}(\mathbf{k}) = \mathrm{III}_{\mathbf{b}_1,\mathbf{b}_2}(\mathbf{k})\left[f_m(\mathbf{k}) + 2f_c(\mathbf{k})e^{-i\mathbf{k}\cdot\mathbf{r}_0}\cos\left(k_z\frac{\lambda_\ell}{2}\right)\right], \tag{4}$$

$$V_{1T}(\mathbf{k}) = \mathrm{III}_{\mathbf{b}_1,\mathbf{b}_2}(\mathbf{k})\left[f_m(\mathbf{k}) + 2f_c(\mathbf{k})\cos\left(\mathbf{k}\cdot\mathbf{r}_0 + k_z\frac{\lambda_\ell}{2}\right)\right], \tag{5}$$

where f_m and f_c are the atomic scattering factors of the metal and chalcogen atoms, respectively, and $\mathbf{r}_0$ is the in-plane metal-chalcogen bond direction ($\mathbf{r}_0 = \frac{\mathbf{a}_1+\mathbf{a}_2}{3}$). $1H$ denotes monolayer $2H$.

Figure 4 (top) highlights the 3D reciprocal-space structure of several monolayer TMDs. The change in metal-chalcogen coordination drastically changes the Bragg rod structure [Figs. 4(a), 4(c) vs 4(e)], whereas the change in chemical composition alters the contour of the rod intensities [Figs. 4(a) vs 4(c)]. The broken inversion symmetry of the $1H$ structure is represented in the complex phase of Eq. (4) that continuously changes on the Γ_1 Bragg rod along $\hat{\mathbf{k}}_z$ [Figs. 4(a) and 4(c)]—this phase is not measurable from the diffraction amplitude. The $1T$ Γ_1 rods are markedly distinct with strong

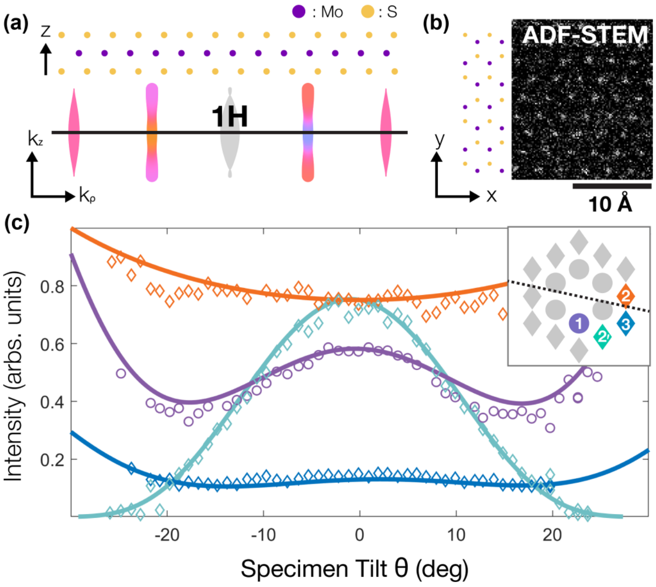

FIG. 5. The k structure of monolayer $2H$-MoS$_2$. The real- and k-space structure of monolayer (a) $2H$-MoS$_2$ polytype shows mirror symmetry distinct from $1T$. However, (b) real-space schematic and ADF-STEM image along $\hat{\mathbf{z}}$ shows classification of $2H$ and $1T$ phase is extremely difficult because Mo atom intensities overwhelm S atoms. (c) Directly probing the rod structure, the experimental tilt pattern shows clear mirror symmetry and shows good agreement with the $2H$ analytic model. Rod intensity is plotted against k_z in Fig. S7 of the Supplemental Material [26].

asymmetric oscillation of amplitude. We see that similarly to graphene, TMDs possess Γ_2 rods symmetric about $k_z = 0$ and insensitive to chalcogen coordination.

The experimental tilt pattern of an exfoliated MoS$_2$ flake shown in Fig. 5 reveals a single-layer H phase. The Γ_1 and Γ_3 curves [Fig. 5(c) (purple, blue)] are symmetric about $\theta = 0$ degrees, which indicates a mirror plane at $k_z = 0$. This feature clearly discerns monolayers of the $2H$ and $1T$ polytypes (see also Figs. S3 and S5 of the Supplemental Material [26]). The kinematic model of monolayer $2H$-MoS$_2$ closely matches the experimental result [Fig. 5(c)]. Although monolayer $2H$ and $1T$ phases have different projected structure in real space, the light sulfur atoms are virtually invisible in high-angle annular dark field (HAADF) STEM, making this distinction challenging to characterize in real space [Fig. 5(b)].

The intralayer spacing in a 2D TMD is precisely quantified by diffraction tilt patterns for the first time. Nonlinear regression analysis of the experimental monolayer $2H$-MoS$_2$ data reveals an intralayer chalcogen-chalcogen spacing (λ_ℓ) of 3.07 Å with a 95% confidence interval of ±0.11 Å based on a kinematic model. Multiple scattering may further reduce precision, especially in thicker systems containing strong scatterers. Our single-layer value is comparable to the previously reported 3.01 Å for bulk $2H$-MoS$_2$ [38].

The addition of a second vdW layer opens a wider range of stacking configurations and the Bragg rod complexity expands quickly—with three Fourier coefficients per vdW layer. Most notably, the bilayer gains a beat frequency described by the interlayer spacing, λ_L. The interlayer beating is concisely expressed for bilayer $1T$: $V_{2T}(\mathbf{k}) = V_{1T}(\mathbf{k}) \cdot 2\cos(k_z \frac{\lambda_L}{2})$. The rapid rod oscillation from the larger vdW gap ($\lambda_L > \lambda_\ell$) beats with intralayer oscillations to create a nonuniform spacing between amplitude minima and maxima.

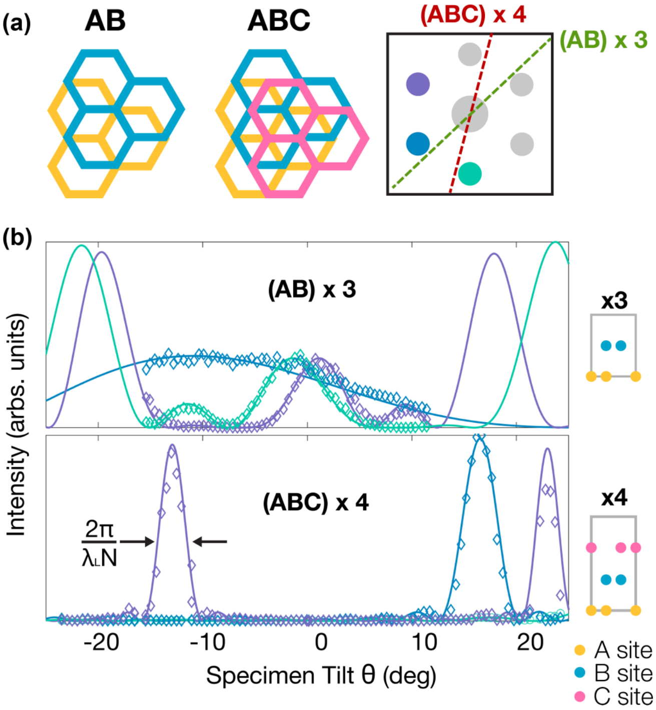

FIG. 6. Diffraction tilt patterns of multilayer Bernal and rhombohedral graphene. (a) Real-space stacking of Bernal (AB) and rhombohedral (ABC) graphene layers. (b) Experimental diffraction tilt patterns are plotted along with matched kinematically modeled patterns. Top right inset labels the plotted Bragg rods and specimen tilt axis. Rod intensity is plotted against k_z in Fig. S7 of the Supplemental Material [26].

Additionally, multilayer TMDs have several stacking geometries both within and between their vdW layers. For instance, $2H$-MoS$_2$ and $2H$-TaSe$_2$ have distinct structures, typically denoted as $2H$(b) and $2H$(a), respectively [Figs. 4(b) and 4(d)]. The Bragg rod structures for single-layer and bilayer T and H phases are shown in Fig. 4. Figure S3 of the Supplemental Material [26] provides an atlas of TMD stacking geometries and illustrates the distinct structures in k space that allow unique identification and quantification.

VII. MULTILAYER 2D MATERIALS

Here we use multilayer graphene to illustrate how diffraction tilt patterns can characterize thicker 2D materials. In atomically registered multilayer graphene, there are three possible sublattice positions—A, B, C—each one bond length apart from the others [Fig. 6(a)]. The two ordered stackings, hexagonally symmetric AB (Bernal) and rhombohedrally symmetric ABC, have been shown to have dramatically different band structures and transport properties [39,40]. However, thickness and stacking-order determination is particularly difficult for samples more than three layers thick. In bulk materials, the rods give way to discrete peaks along $\hat{\mathbf{k}}_z$ (Fig. S1 of the Supplemental Material [26]), but at intermediate thicknesses (3–15 layers) they still contain interpretable out-of-plane structural information. Although the possible stacking configurations grow exponentially with thickness, leveraging minimal prior knowledge about the specimen significantly reduces the number of possibilities and makes exact determination of structure tractable.

Here, we characterize the out-of-plane structure of mechanically exfoliated 6- and 12-layer graphene samples. At these intermediate thicknesses, the number of graphene layers is redundantly described by the width of each Bragg rod along $\hat{\mathbf{k}}_z$ ($\Delta k_z = \frac{2\pi}{\lambda_L N}$), the angle at which the second-order peak first reaches zero while tilting with an axis of rotation along Γ_1 ($N = \frac{21}{\theta(deg)}$), and the intensity of the second-order Bragg rod ($I = 4\frac{\sin^2(1/2)k_z\lambda_L N}{\sin^2(1/2)k_z\lambda_L}$). These three relationships are derived in Sec. IV of the Supplemental Material [26] from analytic models of multilayer graphene.

By measuring the relative intensity of the first- and second-order Bragg peaks ($|\Gamma_1/\Gamma_2|$) at zero tilt ($k_z = 0$), we can determine the fraction of each sublattice in the system. For instance, with equal number of all three sublattices' layers (e.g., ABCABC) the first-order Bragg peaks have zero intensity; if the system has only two sublattices' layers in equal number (e.g., ABAB) the relative intensity is 0.25 (Sec. VI of the Supplemental Material [26]).

Applying these rules to the tilt pattern in Fig. 6(b) (top), we determined the sample has six layers and an equal number of A and B sublattices. Registered six-layer graphene has 3^5 possible configurations. Eliminating the trivial duplicates and those with incorrect sublattice proportions leaves only seven possible stacking orders from which we matched the correct stacking—ABABAB—by comparison with kinematically modeled tilt patterns.

Likewise, the sample in Fig. 6(b) (bottom) was found to be 12 layers thick with an equal proportion of A, B, and C sublattices, allowing the stacking order to be classified as ABCABCABCABC, the rhombohedral ordered stacking. Fast identification of rhombohedral graphene may have importance in fabrication of 2D heterostructure devices.

VIII. SUMMARY AND CONCLUSION

Dimensionally confined 2D materials have rich 3D structure in reciprocal space described by nearly infinite Bragg rods that oscillate with complex magnitude encoding the out-of-plane structure. Using a simple kinematic model of diffraction, combined with specimen tilt, the structure of these Bragg rods has been mapped in detail for several 2D materials (graphene, TMDs) across a range of stacking geometries. Using this 3D diffraction technique, we probed out-of-plane structure and symmetry to quantitatively determine critical structural parameters such as inter- and intralayer spacings and stacking order in multilayer graphene and TMDs. For single-layer MoS_2 we extracted a chalcogen-chalcogen layer spacing of 3.07 ± 0.11 Å. We accurately characterized the full interlayer stacking order of bilayer to multilayer graphene (demonstrated up to 12 layers), as well as identified multilayer rhombohedral graphene. The physical and electronic properties of layered 2D materials are often dramatically susceptible to these parameters. Although efficiently extracted with 3D diffraction, out-of-plane features are challenging or impossible to extract using real-space optical or surface measurement methods. However, our results are obtained using a rudimentary TEM available at most institutions. With the increasing complexity of multilayered materials—engineered by composition, twist, and stacking order—the foundational details outlined in this paper enable rapid and/or high-precision characterization across the complete class of 2D materials. Reciprocal structures illustrated throughout the paper and Supplemental Material [26] provide a 2D materials atlas for 3D diffraction. Furthermore, this work directly empowers a broader range of advanced diffraction based imaging techniques—such as dark-field TEM and 4D STEM—capable of mapping structural order in real space.

ACKNOWLEDGMENTS

The authors thank David A. Muller for useful scientific discussion. S.H.S. and N.S. contributed equally to this work. The authors acknowledge the financial support of the University of Michigan College of Engineering and NSF Grants No. DMR-9871177 and No. DMR-0723032, and technical support from the Michigan Center for Materials Characterization, and made use of the Cornell Center for Materials Research Shared Facilities which are supported through the NSF MRSEC program (DMR-1719875).

---

[1] M. Acerce, D. Voiry, and M. Chhowalla, Metallic 1T phase MoS_2 nanosheets as supercapacitor electrode materials, Nat. Nanotechnol. **10**, 313 (2015).

[2] A. Splendiani, L. Sun, Y. Zhang, T. Li, J. Kim, C.-Y. Chim, G. Galli, and F. Wang, Emerging photoluminescence in monolayer MoS_2, Nano Lett. **10**, 1271 (2010).

[3] E. V. Castro, K. S. Novoselov, S. V. Morozov, N. M. R. Peres, J. M. B. Lopes dos Santos, J. Nilsson, F. Guinea, A. K. Geim, and A. H. Castro Neto, Biased Bilayer Graphene: Semiconductor with a Gap Tunable by the Electric Field Effect, Phys. Rev. Lett. **99**, 216802 (2007).

[4] T. Ohta, A. Bostwick, T. Seyller, K. Horn, and E. Rotenberg, Controlling the electronic structure of bilayer graphene, Science **313**, 951 (2006).

[5] J. R. Schaibley, H. Yu, G. Clark, P. Rivera, J. S. Ross, K. L. Seyler, W. Yao, and X. Xu, Valleytronics in 2D materials, Nat. Rev. Mater. **1**, 16055 (2016).

[6] Y. Cao, V. Fatemi, S. Fang, K. Watanabe, T. Taniguchi, E. Kaxiras, and P. Jarillo-Herrero, Unconventional superconductivity in magic-angle graphene superlattices, Nature (London) **556**, 43 (2018).

[7] P. Blake, E. W. Hill, A. H. Castro Neto, K. S. Novoselov, D. Jiang, R. Yang, T. J. Booth, and A. K. Geim, Making graphene visible, Appl. Phys. Lett. **91**, 063124 (2007).

[8] A. C. Ferrari, J. C. Meyer, V. Scardaci, C. Casiraghi, M. Lazzeri, F. Mauri, S. Piscanec, D. Jiang, K. S. Novoselov, S. Roth, and A. K. Geim, Raman Spectrum of Graphene and Graphene Layers, Phys. Rev. Lett. **97**, 187401 (2006).

[9] K. S. Novoselov, A. K. Geim, S. V. Morozov, D. Jiang, Y. Zhang, S. V. Dubonos, I. V. Grigorieva, and A. A. Firsov, Electric field effect in atomically thin carbon films, Science **306**, 666 (2004).

[10] X. Li, W. Cai, J. An, S. Kim, J. Nah, D. Yang, R. Piner, A. Velamakanni, I. Jung, E. Tutuc, S. K. Banerjee, L. Colombo, and R. S. Ruoff, Large-area synthesis of high-quality and uniform graphene films on copper foils, Science **324**, 1312 (2009).

[11] N. Alem, Q. M. Ramasse, C. R. Seabourne, O. V. Yazyev, K. Erickson, M. C. Sarahan, C. Kisielowski, A. J. Scott, S. G. Louie, and A. Zettl, Subangstrom Edge Relaxations Probed by Electron Microscopy in Hexagonal Boron Nitride, Phys. Rev. Lett. **109**, 205502 (2012).

[12] P. Y. Huang, C. S. Ruiz-Vargas, A. M. van der Zande, W. S. Whitney, M. P. Levendorf, J. W. Kevek, S. Garg, J. S. Alden, C. J. Hustedt, Y. Zhu, J. Park, P. L. McEuen, and D. A. Muller, Grains and grain boundaries in single-layer graphene atomic patchwork quilts, Nature (London) **469**, 389 (2011).

[13] L. Brown, R. Hovden, P. Huang, M. Wojcik, D. A. Muller, and J. Park, Twinning and twisting of tri- and bilayer graphene, Nano Lett. **12**, 1609 (2012).

[14] J. Ping and M. S. Fuhrer, Layer number and stacking sequence imaging of few-layer graphene by transmission electron microscopy, Nano Lett. **12**, 4635 (2012).

[15] C.-J. Kim, L. Brown, M. W. Graham, R. Hovden, R. W. Havener, P. L. McEuen, D. A. Muller, and J. Park, Stacking order dependent second harmonic generation and topological defects in h-BN bilayers, Nano Lett. **13**, 5660 (2013).

[16] L. de Broglie, Recherches sur la théorie des quanta, Ann. Phys. (Paris) **10**, 22 (1925).

[17] G. P. Thomson and A. Reid, Diffraction of cathode rays by a thin film, Nature (London) **119**, 890 (1927).

[18] C. J. Davisson and L. H. Germer, Reflection of electrons by a crystal of nickel, Proc. Natl. Acad. Sci. USA **14**, 317 (1928).

[19] P. B. Hirsch, A. Howie, and M. J. Whelan, A kinematical theory of diffraction contrast of electron transmission microscope images of dislocations and other defects, Philos. Trans. R. Soc. London A **252**, 499 (1960).

[20] K. Iakoubovskii, K. Mitsuishi, Y. Nakayama, and K. Furuya, Mean free path of inelastic electron scattering in elemental solids and oxides using transmission electron microscopy: Atomic number dependent oscillatory behavior, Phys. Rev. B **77**, 104102 (2008).

[21] A. L. G. Rees and J. A. Spink, The shape transform in electron diffraction by small crystals, Acta Crystallogr. **3**, 316 (1950).

[22] J. M. Cowley, A. L. G. Rees, and J. A. Spink, The morphology of zinc oxide smoke particles, Proc. Phys. Soc. B **64**, 638 (1951).

[23] M. Henzler, Spot profile analysis (LEED) of defects at silicon surfaces, Surf. Sci. **132**, 82 (1983).

[24] M. G. Lagally, D. E. Savage, and M. C. Tringides, Diffraction from disordered surfaces: An overview, in *Reflection High-Energy Electron Diffraction and Reflection Electron Imaging of Surfaces*, edited by P. K. Larsen and P. J. Dobson (Springer US, Boston, MA, 1988), pp. 139–174.

[25] I. K. Robinson, Crystal truncation rods and surface roughness, Phys. Rev. B **33**, 3830 (1986).

[26] See Supplemental Material at http://link.aps.org/supplemental/10.1103/PhysRevMaterials.3.064003 for additional details on experimental methods, formulation of real and reciprocal space 2D lattices, reciprocal space parametrization, sublattice selection rules, and an atlas of reciprocal space structures and tilt patterns for graphene and transition metal dichalcogenides.

[27] J. C. Meyer, A. K. Geim, M. I. Katsnelson, K. S. Novoselov, T. J. Booth, and S. Roth, The structure of suspended graphene sheets, Nature (London) **446**, 60 (2007).

[28] A. M. Popov, I. V. Lebedeva, A. A. Knizhnik, Y. E. Lozovik, and B. V. Potapkin, Commensurate-incommensurate phase transition in bilayer graphene, Phys. Rev. B **84**, 045404 (2011).

[29] J. D. Bernal, The structure of graphite, Proc. R. Soc. London A **106**, 749 (1924).

[30] P. P. Ewald, Die Berechnung optischer und elektrostatischer Gitterpotentiale, Ann. Phys. (Berlin) **369**, 253 (1921).

[31] G. Friedel, Sur les symétries cristallines que peut révéler la diffraction des rayons Röntgen, C. R. Acad. Sci. **157**, 1533 (1913).

[32] H. Fang, C. Battaglia, C. Carraro, S. Nemsak, B. Ozdol, J. S. Kang, H. A. Bechtel, S. B. Desai, F. Kronast, A. A. Unal, G. Conti, C. Conlon, G. K. Palsson, M. C. Martin, A. M. Minor, C. S. Fadley, E. Yablonovitch, R. Maboudian, and A. Javey, Strong interlayer coupling in van der Waals heterostructures built from single-layer chalcogenides, Proc. Natl. Acad. Sci. USA **111**, 6198 (2014).

[33] E. J. Mele, Commensuration and interlayer coherence in twisted bilayer graphene, Phys. Rev. B **81**, 161405(R) (2010).

[34] H. Yoo, R. Engelke, S. Carr, S. Fang, K. Zhang, P. Cazeaux, S. H. Sung, R. Hovden, A. W. Tsen, T. Taniguchi, K. Watanabe, G.-C. Yi, M. Kim, M. Luskin, E. B. Tadmor, E. Kaxiras, and P. Kim, Atomic reconstruction at van der Waals interface in twisted bilayer graphene, Nat. Mater. **18**, 448 (2019).

[35] R. Hovden, A. W. Tsen, P. Liu, B. H. Savitzky, I. El Baggari, Y. Liu, W. Lu, Y. Sun, P. Kim, A. N. Pasupathy, and L. F. Kourkoutis, Atomic lattice disorder in charge-density-wave phases of exfoliated dichalcogenides (1T-TaS$_2$), Proc. Natl. Acad. Sci. USA **113**, 11420 (2016).

[36] J. A. Wilson and A. D. Yoffe, The transition metal dichalcogenides discussion and interpretation of the observed optical, electrical and structural properties, Adv. Phys. **18**, 193 (1969).

[37] B. Sipos, A. F. Kusmartseva, A. Akrap, H. Berger, L. Forró, and E. Tutiš, From Mott state to superconductivity in 1T-TaS$_2$, Nat. Mater. **7**, 960 (2008).

[38] B. Schönfeld, J. J. Huang, and S. C. Moss, Anisotropic mean-square displacements (MSD) in single-crystals of 2H- and 3R-MoS$_2$, Acta Crystallogr. Sect. B **39**, 404 (1983).

[39] R. Xiao, F. Tasnádi, K. Koepernik, J. W. F. Venderbos, M. Richter, and M. Taut, Density functional investigation of rhombohedral stacks of graphene: Topological surface states, nonlinear dielectric response, and bulk limit, Phys. Rev. B **84**, 165404 (2011).

[40] W. Bao, L. Jing, J. Velasco Jr., Y. Lee, G. Liu, D. Tran, B. Standley, M. Aykol, S. B. Cronin, D. Smirnov, M. Koshino, E. McCann, M. Bockrath, and C. N. Lau, Stacking-dependent band gap and quantum transport in trilayer graphene, Nat. Phys. **7**, 948 (2011).